Nanoarray Catalysts

DOI: 10.1002/anie.201403461

# Monolithically Integrated Spinel $M_xCo_{3-x}O_4$ (M = Co, Ni, Zn) Nanoarray Catalysts: Scalable Synthesis and Cation Manipulation for Tunable Low-Temperature $CH_4$ and CO Oxidation**

*Zheng Ren, Venkatesh Botu, Sibo Wang, Yongtao Meng, Wenqiao Song, Yanbing Guo, Ramamurthy Ramprasad, Steven L. Suib, and Pu-Xian Gao**

***Abstract:*** *A series of large scale $M_xCo_{3-x}O_4$ (M = Co, Ni, Zn) nanoarray catalysts have been cost-effectively integrated onto large commercial cordierite monolithic substrates to greatly enhance the catalyst utilization efficiency. The monolithically integrated spinel nanoarrays exhibit tunable catalytic performance (as revealed by spectroscopy characterization and parallel first-principles calculations) toward low-temperature CO and $CH_4$ oxidation by selective cation occupancy and concentration, which lead to controlled adsorption–desorption behavior and surface defect population. This provides a feasible approach for scalable fabrication and rational manipulation of metal oxide nanoarray catalysts applicable at low temperatures for various catalytic reactions.*

The increasingly stringent environmental regulations for CO, $NO_x$, HC, and particulate matter (PM) emissions from mobile and stationary sources call for the development of new and highly efficient catalysts.[1] Meanwhile, clean and fuel-efficient low-temperature combustion (LTC) have held great promise in the pursuit of highly efficient engine-, combustor-, and turbine-based energy devices, prompting the urgent need for low-cost, efficient, and robust catalytic emission control devices at low temperature. The state-of-the-art platinum-group metal (PGM)-based emission-control catalysts rely on the significant usage of PGM (ca. 1 wt% loading) with a large amount of support washcoat, such as mesoporous $Al_2O_3$ microparticles on monolithic substrates, which generally account for circa 20–200 μm thick coatings on the monolith channel walls. The commercial catalytic post-treatment devices in automobiles (catalytic converters) integrate the bare monoliths with highly porous metal oxide supports and catalysts with high surface area and activity.[2] The bare monoliths are constructed with parallel or honeycomb channels of about 1 mm in diameter. Practically, the metal oxide support or catalyst loading involves a less-than-ideal washcoating process owing to the lack of effective control over the physical and chemical structure of the catalysts, substrate adherence, dispersion, and optimum materials utilization efficiency. Recently, we have successfully invented and demonstrated the integration of 3D catalytic metal oxide nanoarrays onto channeled monolithic substrates.[3] These monolithic nanoarray catalysts were shown to reduce the catalyst usage by 10–40 times without sacrificing the catalytic performance.[3a] The nanoarray architecture offers advantages of structural stability under high temperature or mechanical agitations, and high surface area to facilitate gas–solid interactions promoting catalytic activity.[3,4] Despite the merits these nanoarray catalysts could bring, the industrially relevant scale-up is required for bridging this nanotechnology with realistic industrial application. Herein, we report for the first time the scalable integration of nanoarrays onto large commercial monolithic honeycombs (Figure 1), which can be directly used as structured oxidation catalysts. Through rational alloying with transition metals, such as Ni and Zn, the cation populations and occupancies in spinel cobalt oxide, a high performance oxidation catalyst[4,5] has been successfully created to tune the catalytic activity towards different oxidation reactions at low temperature.

We started with a urea hydrolysis process to first prepare basic carbonate nanowire arrays and the spinel cobaltite $M_xCo_{3-x}O_4$ nanoarrays (M = Co, Zn, Ni; $x = 0.5$) were obtained after ambient annealing at 300 °C. To guarantee a uniform deposition of nanowire arrays inside the long channels, mechanical agitation by a rotating stirring bar was used to promote the mass transfer during the synthesis. Scanning electron microscope (SEM) images in Figure 2 show that the nanowire arrays are uniformly distributed inside the monolithic honeycomb channels. The nanowires are around 10 μm in length. X-ray diffraction (XRD) patterns in the Supporting Information, Figure S1 confirm the formation of spinel cobaltite without phase segregation. Using cordierite honeycomb substrate (JCPDS: 120303) as the reference, the diffraction peak shifts due to the introduction of Zn and Ni can be calculated, and the shift towards lower diffraction angle reveals an increase in the lattice parameter after partial replacement of Co atoms by Zn and Ni. Transmission electron microscopy (TEM) characterization in Figure 1c shows the nanowires are porous in nature. The measured interplanar spacing in Figure 1d corresponds to {111} planes of $Co_3O_4$ and the zone axis is determined to be $\langle 1\bar{1}0\rangle$ based on crystallo-

[*] Z. Ren, V. Botu, S. Wang, Dr. Y. Guo, Prof. Dr. R. Ramprasad, Prof. Dr. P.-X. Gao
Department of Materials Science and Engineering & Institute of Materials Science, University of Connecticut
97 N. Eagleville Road, Storrs, CT (USA)
E-mail: puxian.gao@ims.uconn.edu
Y. Meng, W. Song, Prof. Dr. S. L. Suib
Department of Chemistry & Institute of Materials Science, University of Connecticut
55 N. Eagleville Road, Storrs, CT (USA)

[**] We are grateful for the financial support from the US Department of Energy and the National Science Foundation.

Supporting information for this article is available on the WWW under http://dx.doi.org/10.1002/anie.201403461.

  

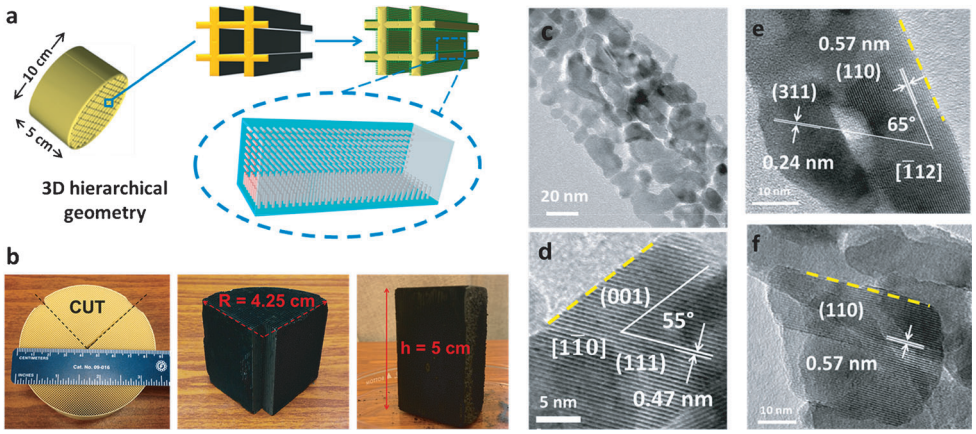


***Figure 1.*** a) Monolithic integration of nanoarrays on commercialized honeycomb supports; b) Photographs of a piece of monolithic nanoarray catalyst; c) TEM characterization of the $Co_3O_4$ nanorrays; HRTEM investigation of d) $Co_3O_4$, e) $Ni_{0.5}Co_{2.5}O_4$, and f) $Zn_{0.5}Co_{2.5}O_4$ nanoarrays.

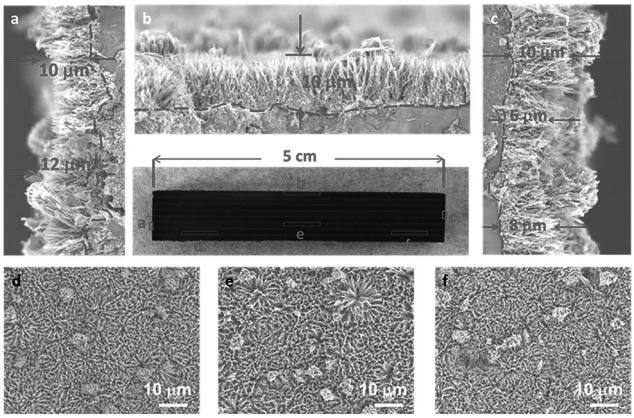


***Figure 2.*** Large-area SEM investigation of the nanoarrays grown inside the monolithic honeycomb channels, revealing a uniform coverage of nanowires (circa 10 μm in length) was achieved throughout the 5 cm long honeycomb channels.

graphic relations. The grain exposes the {110} surfaces that are perpendicular to the $\langle 1\bar{1}0\rangle$ directions owing to the cubic structured cobaltites. Figure 1e and f show that in both Zn and Ni substituted cobalt oxides, the major exposed crystal facets are also {110}. EDS characterization of several nanowires under TEM (Supporting Information, (Figure S2) confirms the ratio of both Zn/Co and Ni/Co to be 1:5. Ammonium fluoride ($NH_4F$) is required for the preparation of $Zn_{0.5}Co_{2.5}O_4$ nanowire arrays. Without the use of $NH_4F$, phase segregation happens as indicated in the Supporting Information, Figure S4 leading to no controlled nanowire morphology.

Figure 3 shows the $Ni_{0.5}Co_{2.5}O_4$ and $Co_3O_4$ nanoarrays exhibit the best methane combustion and CO oxidation performance, respectively. The Ni substitution leads to the total oxidation of methane at temperature lower than 600 °C with only about 15 mg catalytic material usage (See the Supporting Information for details). Neither Ni nor Zn substitution contribute to better CO oxidation activity. The incorporation of Ni, however, promotes $CH_4$ conversion. Arrhenius plots reveal the $Zn_{0.5}Co_{2.5}O_4$ nanoarrays have the largest calculated apparent activation energy for both $CH_4$ combustion and CO oxidation. Density functional theory (DFT) calculation were used to determine the substitution energy of Zn and Ni in $Co_3O_4$, leading to $Zn_{0.5}Co_{2.5}O_4$ and $Ni_{0.5}Co_{2.5}O_4$. $Co_3O_4$ exists in a spinel structure with $Co^{2+}$ at the tetrahedral sites, whereas $Co^{3+}$ occupies the octahedral sites coordinating with O atoms. Figure 4a shows that the substitution by Zn is only favored in the tetrahedral sites, as the substitution energy is positive in the octahedral sites. However, the preference of Ni occupying the tetrahedral (−0.81 eV) over the octahedral sites (−0.72 eV) is marginal based on thermodynamic considerations. Raman spectra of $Ni_{0.5}Co_{2.5}O_4$ and $Co_3O_4$ are shown in Figure 4b. The high-frequency mode located within 650–700 $cm^{-1}$ corresponds to the vibrational modes of octahedral $Co^{3+}$ while the mode at about 200 and 400 $cm^{-1}$ is characteristic of tetrahedral $Co^{2+}$.[6] With decreased population of this high-frequency band and retained intensity of tetrahedral $Co^{2+}$ in Figure 4b, Ni substitutes for Co in the octahedral sites. From previous TEM characterization, the spinel cobaltite nanowires mainly expose {110} planes, which were reported to be the active planes for catalytic oxidation reactions.[5a,c,7] The {110} planes were thus selected for further surface reaction investigations. There are two types of {110} surfaces as depicted in Figure 4a. The type A surfaces only consist of octahedral sites while the type B surfaces have both octahedral and tetrahedral sites. As

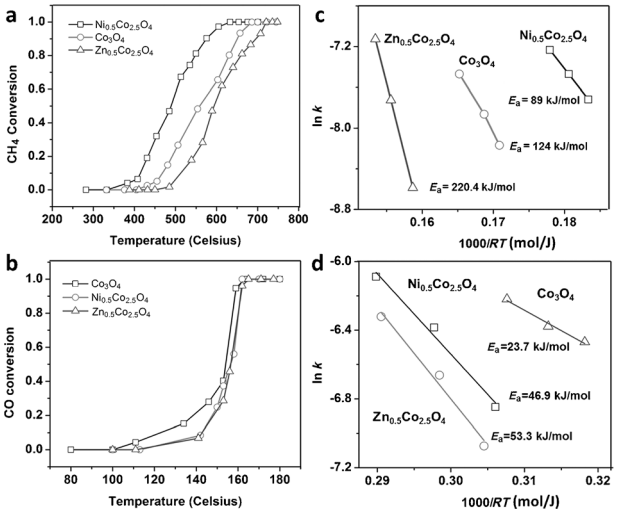


***Figure 3.*** a) Catalytic methane combustion and b) CO oxidation performance of $M_{0.5}Co_{2.5}O_4$ (M = Co, Ni, and Zn) nanoarray catalyst and c), d) the corresponding Arrhenius plots for the reaction kinetics.

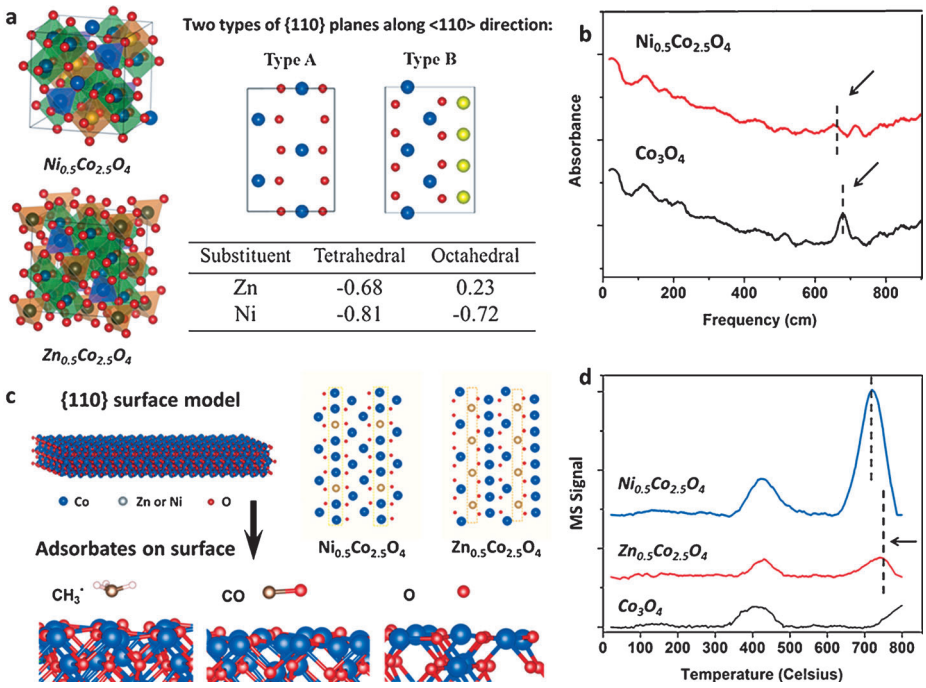


***Figure 4.*** a) Crystal structure determination of $Ni_{0.5}Co_{2.5}O_4$ and $Zn_{0.5}Co_{2.5}O_4$ by DFT calculation of the substitution energy [eV] of Ni and Zn; b) Raman spectra of $Co_3O_4$ and $Ni_{0.5}Co_{2.5}O_4$; c) The surface construction and adsorption energy computation; d) $O_2$-TPD spectra of $Co_3O_4$, $Ni_{0.5}Co_{2.5}O_4$ and $Zn_{0.5}Co_{2.5}O_4$.

Zn is only likely to replace tetrahedral Co atoms, only type B sites were simulated for $Zn_{0.5}Co_{2.5}O_4$, and both types of surfaces were considered for $Ni_{0.5}Co_{2.5}O_4$. For catalytic hydrocarbon combustion, early studies suggest that dissociative adsorbed oxygen determines the low-temperature activity (Eley–Rideal mechanism),[8] while some recent reports propose lattice oxygen is involved.[4c,9] To clarify which mechanism dominates, we first calculate the oxygen adsorption energy on the {110} surface of cobaltite. As summarized in Table 1, the O adsorption energy on tetrahedral Zn is positive (0.48 eV), indicating that Zn substitution suppresses oxygen adsorption compared to oxygen adsorption at a Co (−0.96 eV) site. Ni (−0.23 eV) is also not as favorable. This result corresponds quite well to the temperature-programmed oxygen desorption ($O_2$-TPD) spectrum in Figure 4d with no desorption shoulder observed for $Zn_{0.5}Co_{2.5}O_4$ at temperatures below 300 °C, where most molecular and dissociatively adsorbed oxygen desorb. The peaks located at around 400 °C represent the surface lattice oxygen desorption. The surface lattice oxygen of $Ni_{0.5}Co_{2.5}O_4$ is found to be the most active while that of $Co_3O_4$ is slightly more active than $Zn_{0.5}Co_{2.5}O_4$. The surface lattice oxygen activity from $O_2$-TPD has the same tendency with the catalytic methane combustion activity. Moreover, as shown in Figure 3a, the catalytic methane conversion starts at temperatures higher than 350 °C where dissociative oxygen is less likely to adsorb, surface lattice oxygen dominates in the catalytic methane combustion.

***Table 1:*** DFT calculations of binding energies [eV] for adsorbates on different sites of {110} surfaces.

| Adsorbates | Sites | $Zn_{0.5}Co_{2.5}O_4$ Type B | $Ni_{0.5}Co_{2.5}O_4$ Type A | $Ni_{0.5}Co_{2.5}O_4$ Type B |
|---|---|---|---|---|
| O | Co | −1.85 | 0.11 | −0.96 |
| O | Zn | 0.48 | – | – |
| O | Ni | – | 0.47 | −0.23 |
| CO | Co | −2.53 | −1.69 | −2.5 |
| CO | Zn | −1.18 | – | – |
| CO | Ni | – | −1.28 | −2.59 |
| $CH_3$ | Co | −2.03 | −1.66 | −1.66 |
| $CH_3$ | Zn | −2.29 | – | – |
| $CH_3$ | Ni | – | −1.01 | −1.56 |
| $CH_3$ | O | −1.62 | −2.3 | −1.31 |
| H | O | −3.04 | −3.18 | −2.77 |
| H | Co | −2.79 | −1.91 | −1.08 |
| H | Zn | −2.42 | – | – |
| H | Ni | – | −1.65 | −0.78 |

Catalytic $CH_4$ combustion usually begins with C–H bond activation where the activated H is attacked by oxygen on the catalyst surface.[10] Furthermore, DFT results shown in Table 1 suggest that H has a much a stronger affinity towards surface oxygen than $CH_3$, and $CH_3$ has more negative adsorption energy on metal sites than on surface oxygen sites. Therefore when H is adsorbed on surface oxygen, the $CH_3$ radicals prefer to sit on metal active sites (Co, Ni, and Zn). The calculated binding energy reveals $CH_3$ is most stable on Zn and least stable on Ni. For total oxidation of methane, however, the desorption and further oxidation of $CH_3$ by either lattice or atmospheric oxygen are keys to the reaction rate. In this regard, Ni can facilitate $CH_3$ desorption and this also explains why $Ni_{0.5}Co_{2.5}O_4$ exhibits better activity. Despite the fact that $Zn_{0.5}Co_{2.5}O_4$ is confirmed to be least active, it has a much larger activation energy compared with $Ni_{0.5}Co_{2.5}O_4$ and $Co_3O_4$. This may be ascribed to the poisoning effect of fluorine, a typical halogen ion that deteriorates catalyst activity,[11] which results from the use of $NH_4F$ during the nanowire synthesis. Similar halogen poisoning of Cl has been observed in our previous work, where $Co_3O_4$ prepared from $CoCl_2$ exhibited worse activity towards NO oxidation.[4a] For catalytic CO oxidation on $Co_3O_4$, however, the reaction mechanism has been well-studied. Based on the Mars Van Krevelen mechanism, the CO molecules first adsorb to metal active sites extracting adjacent lattice oxygen to form $CO_2$ and desorb leaving oxygen vacancies.

The lattice oxygen is further regenerated by atmospheric $O_2$. The DFT calculations show both Zn and Ni are not favorable for CO adsorption on type A {110} surfaces. For type B {110} surfaces in $Ni_{0.5}Co_{2.5}O_4$, however, the CO

  

adsorption energy is similar for Ni and Co. A detailed study on Ni substitution is thus necessary to interpret the CO adsorption and to elucidate why the Ni incorporation leads to active surface lattice oxygen favorable for catalytic $CH_4$ combustion.

A series of Ni-substituted cobalt oxide ($Ni_xCo_{3-x}O_4$, $0.27 < x < 1.5$) nanoarrays were prepared by the same hydrothermal processing. Figure 5a illustrates the X-ray photoelectron spectroscopy (XPS) results of O 1s signals for $Ni_xCo_{3-x}O_4$. The broad peaks can be deconvoluted into four major components (lattice oxygen, surface OH group, defective oxygen, and adsorbed moisture). Quantitative analysis (Supporting Information, Table S3) reveals the surface defective oxygen population increases from 14% to 22% as more Ni is incorporated. Meanwhile the surface lattice oxygen population decreases from 49% to 38%. Such a sequence of defective oxygen to lattice oxygen ratio corresponds perfectly with the activity of methane combustion shown in Figure 5b–d. With high defective oxygen to lattice oxygen ratio on the surface, the mobility of surface lattice oxygen can be greatly improved. As an oxide catalyst for hydrocarbon combustion, the higher lattice oxygen mobility usually leads to higher catalytic activity. A similar behavior has been reported in other oxides and perovskites for hydrocarbon combustion.[12] For catalytic CO oxidation, however, the deficiency in surface lattice oxygen leads to the slower $CO_2$ formation and desorption, which lowers the catalytic activity.

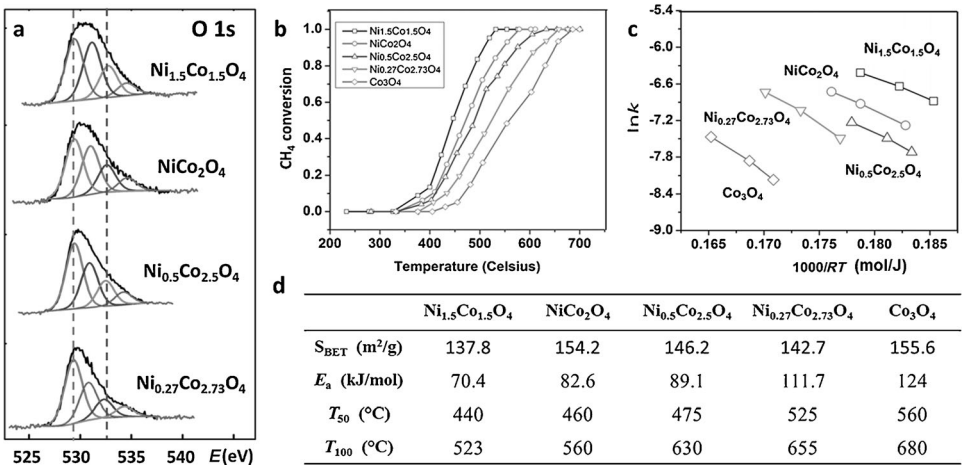


| | $Ni_{1.5}Co_{1.5}O_4$ | $NiCo_2O_4$ | $Ni_{0.5}Co_{2.5}O_4$ | $Ni_{0.27}Co_{2.73}O_4$ | $Co_3O_4$ |
|---|---|---|---|---|---|
| $S_{BET}$ ($m^2$/g) | 137.8 | 154.2 | 146.2 | 142.7 | 155.6 |
| $E_a$ (kJ/mol) | 70.4 | 82.6 | 89.1 | 111.7 | 124 |
| $T_{50}$ (°C) | 440 | 460 | 475 | 525 | 560 |
| $T_{100}$ (°C) | 523 | 560 | 630 | 655 | 680 |

***Figure 5.*** a) XPS spectra of $Ni_xCo_{3-x}O_4$ with different Ni/Co ratios; b) enhanced methane combustion with higher Ni concentration; c) Arrhenius plots of $Ni_xCo_{3-x}O_4$ for methane combustion; d) summary of surface area, apparent activation energy, and characteristic reaction temperatures of $Ni_xCo_{3-x}O_4$.

For cobaltite catalyst application in combustion technology, another issue is thermal stability. Stability results of $Ni_{0.5}Co_{2.5}O_4$ (Supporting Information, Figure S6) show that Ni incorporation leads to increased stability at low conversion rate, while at high conversion the stability remains similar. However, $NiCo_2O_4$ was found to decompose at temperature higher than 400°C, producing a small amount of NiO precipitation and $Ni_xCo_{3-x}O_4$ matrix.[13] As shown in Figure 4d, the bulk lattice oxygen desorbs at a lower temperature (ca. 750°C) after Ni and Zn are introduced to the spinel lattice. The desorption peak indicates $Ni_{0.5}Co_{2.5}O_4$ is less stable than $Zn_{0.5}Co_{2.5}O_4$. Further investigation by XRD reveals $Ni_xCo_{3-x}O_4$ annealed at 400°C, 500°C and 600°C are stable without thermal decomposition when $x < 0.5$ (Supporting Information, Figure S12) which thus makes $Ni_xCo_{3-x}O_4$ nanoarrays ($x < 0.5$) suitable for low temperature catalytic methane combustion. Although the catalytic activity can be enhanced by Ni alloying, the increased Ni concentration ($x > 0.5$) deteriorates the thermal stability of $Ni_xCo_{3-x}O_4$ with NiO precipitation. It is thus of necessity to balance the increased catalytic conversion efficiency and the possible operation-temperature-induced thermal decomposition when $Ni_xCo_{3-x}O_4$ is used for catalytic hydrocarbon combustion.

In summary, a series of large-scale $Co_3O_4$-based nanoarray catalysts have been cost-effectively integrated onto large commercial cordierite monolithic substrates with controlled substitution alloying of various cations such as Zn and Ni. The monolithically integrated spinel nanoarrays exhibit tunable catalytic performance toward low temperature CO and $CH_4$ oxidation by selective cations occupancy and concentration, which lead to adjusted adsorption–desorption behavior and surface defect population. This may provide a feasible approach of scalable fabrication and rational manipulation of nanoarrays for various catalytic oxidation reactions towards lower temperature.

Received: March 18, 2014
Revised: April 23, 2014
Published online: May 30, 2014

**Keywords:** density functional calculations · heterogeneous catalysis · low-temperature oxidation · nanoarrays · scalable synthesis

[1] a) J. Lin, B. Qiao, J. Liu, Y. Huang, A. Wang, L. Li, W. Zhang, L. F. Allard, X. Wang, T. Zhang, *Angew. Chem.* **2012**, *124*, 2974–2978; *Angew. Chem. Int. Ed.* **2012**, *51*, 2920–2924; b) X. Mou, B. Zhang, Y. Li, L. Yao, X. Wei, D. S. Su, W. Shen, *Angew. Chem.* **2012**, *124*, 3044–3048; *Angew. Chem. Int. Ed.* **2012**, *51*, 2989–2993; c) M. He, Y. Sun, B. Han, *Angew. Chem.* **2013**, *125*, 9798–9812; *Angew. Chem. Int. Ed.* **2013**, *52*, 9620–9633; d) M. Cargnello, J. J. D. Jaén, J. C. H. Garrido, K. Bakhmutsky, T. Montini, J. J. C. Gámez, R. J. Gorte, P. Fornasiero, *Science* **2012**, *337*, 713–717.
[2] J. L. Williams, *Catal. Today* **2001**, *69*, 3–9.
[3] a) Y. Guo, Z. Ren, W. Xiao, C. Liu, H. Sharma, H. Gao, A. Mhadeshwar, P.-X. Gao, *Nano Energy* **2013**, *2*, 873–881; b) W. Xiao, Y. Guo, Z. Ren, G. Wrobel, Z. Ren, T. Lu, P.-X. Gao, *Cryst.*

  

*Growth Des.* **2013**, *13*, 3657 – 3664; c) Y. Guo, G. Liu, Z. Ren, A. Piyadasa, P.-X. Gao, *CrysEngComm* **2013**, *15*, 8345 – 8352.

[4] a) Z. Ren, Y. Guo, Z. Zhang, C. Liu, P.-X. Gao, *J. Mater. Chem. A* **2013**, *1*, 9897 – 9906; b) J. Sun, Y. Li, X. Liu, Q. Yang, J. Liu, X. Sun, D. G. Evans, X. Duan, *Chem. Commun.* **2012**, *48*, 3379 – 3381; c) Y. Feng, P. M. Rao, D. R. Kim, X. Zheng, *Proc. Combust. Inst.* **2011**, *33*, 3169 – 3175; d) Y. Feng, X. Zheng, *ChemCatChem* **2012**, *4*, 1551 – 1554; e) Y. Feng, X. Zheng, *Nano Lett.* **2010**, *10*, 4762 – 4766.

[5] a) X. W. Xie, Y. Li, Z. Q. Liu, M. Haruta, W. J. Shen, *Nature* **2009**, *458*, 746 – 749; b) L. Hu, Q. Peng, Y. Li, *J. Am. Chem. Soc.* **2008**, *130*, 16136 – 16137; c) L. Hu, K. Sun, Q. Peng, B. Xu, Y. Li, *Nano Res.* **2010**, *3*, 363 – 368.

[6] a) J. Preudhomme, P. Tarte, *Spectrochim. Acta Part A* **1971**, *27*, 1817 – 1835; b) C. F. Windisch, G. J. Exarhos, R. R. Owings, *J. Appl. Phys.* **2004**, *95*, 5435 – 5442.

[7] Y. Xie, F. Dong, S. Heinbuch, J. J. Rocca, E. R. Bernstein, *Phys. Chem. Chem. Phys.* **2010**, *12*, 947 – 959.

[8] a) V. D. Sokolovskii, *Catal. Rev.* **1990**, *32*, 1 – 49; b) S. Pengpanich, V. Meeyoo, T. Rirksomboon, K. Bunyakiat, *Appl. Catal. A* **2002**, *234*, 221 – 233; c) G. Saracco, F. Geobaldo, G. Baldi, *Appl. Catal. B* **1999**, *20*, 277 – 288.

[9] a) N. Bahlawane, *Appl. Catal. B* **2006**, *67*, 168 – 176; b) K.-i. Fujimoto, F. H. Ribeiro, M. Avalos-Borja, E. Iglesia, *J. Catal.* **1998**, *179*, 431 – 442; c) M. Alifanti, J. Kirchnerova, B. Delmon, D. Klvana, *Appl. Catal. A* **2004**, *262*, 167 – 176.

[10] a) R. Burch, D. J. Crittle, M. J. Hayes, *Catal. Today* **1999**, *47*, 229 – 234; b) E. Finocchio, G. Busca, V. Lorenzelli, R. J. Willey, *J. Catal.* **1995**, *151*, 204 – 215.

[11] a) C. H. Bartholomew, *Appl. Catal. A* **2001**, *212*, 17 – 60; b) C. F. Cullis, B. M. Willatt, *J. Catal.* **1984**, *86*, 187 – 200; c) D. O. Simone, T. Kennelly, N. L. Brungard, R. J. Farrauto, *Appl. Catal.* **1991**, *70*, 87 – 100.

[12] a) J. Li, H. Fu, L. Fu, J. Hao, *Environ. Sci. Technol.* **2006**, *40*, 6455 – 6459; b) J. G. McCarty, H. Wise, *Catal. Today* **1990**, *8*, 231 – 248; c) L. F. Liotta, M. Ousmane, G. Di Carlo, G. Pantaleo, G. Deganello, G. Marcì, L. Retailleau, A. Giroir-Fendler, *Appl. Catal. A* **2008**, *347*, 81 – 88.

[13] M. Cabo, E. Pellicer, E. Rossinyol, O. Castell, S. Suriñach, M. D. Baró, *Cryst. Growth Des.* **2009**, *9*, 4814 – 4821.

  